Particle Acceleration in Collisionless Magnetically Arrested Disks

Jesse Vos,[1,*] Benoît Cerutti,[2] Monika Mościbrodzka,[1] and Kyle Parfrey[3]
[1]Department of Astrophysics/IMAPP, Radboud University, P.O. Box 9010, 6500 GL Nijmegen, The Netherlands
[2]Univ. Grenoble Alpes, CNRS, IPAG, 38000 Grenoble, France
[3]Princeton Plasma Physics Laboratory, Princeton, New Jersey 08540, USA

(Received 25 October 2024; revised 10 March 2025; accepted 14 May 2025; published 2 July 2025)

We present the first collisionless realization of two-dimensional axisymmetric black hole accretion consistent with a persistent magnetically arrested disk state. The accretion flow, consisting of an ion-electron disk plasma combined with magnetospheric pair creation effects, is simulated using first-principles general-relativistic particle-in-cell methods. The simulation is evolved over significant dynamical timescales during which a quasisteady accretion state is reached with several magnetic flux eruption cycles. We include a realistic treatment of inverse Compton scattering and pair production, which allows for studying the interaction between the collisionless accretion flow and pair-loaded jet. Our findings indicate that magnetic flux eruptions associated with equatorial magnetic reconnection within the black hole magnetosphere and the formation of spark gaps are locations of maximal particle acceleration. Flux eruptions, starting near the central black hole, can trigger Kelvin-Helmholtz-like vortices at the jet-disk interface that facilitate efficient mixing between disk and jet plasma in this region. Transient periods of increased pair production following magnetic flux eruptions and reconnection events are responsible for most of the highly accelerated particles.

DOI: 10.1103/5wwb-7t2n

Introduction—Supermassive black holes (BH) at the center of low-luminosity active galactic nuclei (LLAGN) accrete ion-lepton plasma whose high temperatures and low densities place it in the collisionless regime [1]. Some of these BHs are known to launch jets, but these features are well established to not be universal [2–4]. Examples can be found in the two LLAGN M87* and Sagittarius A*, where M87* shows a prominent, large-scale jet and Sagittarius A* only displays radiative characteristics typical for a compact jet [5,6]. The Event Horizon Telescope has observed emission structures associated with millimeter-wavelength synchrotron radiation from near-horizon relativistic accretion flows for both systems [7,8]. Although these emission features are likely produced by the bulk accretion flow, the question remains of how and where the higher-energy emission and particles are created.

Many jetted black hole systems, including M87* and Sagittarius A*, display γ-ray activity [9–15]. These systems can go through periods of increased (i.e., flaring) activity [16–18], which can be related to the dynamics of the central engine that drives jet launching mechanics and its associated plasma effects. The source of the high-energy emission is often tied to the collisionless plasma dynamics within the BH magnetosphere, but it remains a challenge to identify the responsible mechanisms and locations. With this numerical study, we therefore aim to simultaneously assess the ability of accretion-driven and magnetospheric processes to accelerate particles to high, nonthermal energies.

The Magnetically Arrested Disk [MAD; [19,20]] state is currently a preferred model for interpreting millimeter emission from the two aforementioned LLAGN, both with regard to the polarimetric signatures [21] and the origin of flares with associated orbital motion of hot spots [22–25]. MAD episodes are characterized by flux eruptions, during which a limiting horizon-penetrating magnetic flux is reached, or even exceeded, resulting in the partial halting of the accretion flow [e.g., [26–31]]. General-relativistic magnetohydrodynamical (GRMHD) models that bring about the MAD state are characterized by large-scale coherent magnetic fields and sizable initialized disk structures. However, GRMHD methods are technically not applicable in the collisionless regime and do not directly provide insight into the nonideal processes associated with particle acceleration. It is therefore valuable to investigate these systems with methods that self-consistently take into account these processes while simultaneously building on the GRMHD findings.

In this Letter, we employ general relativistic (radiative) particle-in-cell [GR(R)PIC] methods to undertake a global collisionless study combining initialized accretion flows

*Contact author: jt.vos@astro.ru.nl

Published by the American Physical Society under the terms of the Creative Commons Attribution 4.0 International license. Further distribution of this work must maintain attribution to the author(s) and the published article's title, journal citation, and DOI.

and particle creation processes. We present a quasisteady, axisymmetric MAD accretion state and focus on interpreting the locations and mechanisms of particle acceleration within this environment. The system's characteristics—highly magnetized, with large-scale coherent field structures—are reminiscent of the well-established MAD state in GRMHD models [e.g., [26–31]]. Previously, several kinetic studies of black hole magnetospheres were undertaken that mostly focused on pair-created plasma dynamics under magnetically dominated conditions [32–38] or spherically symmetric Bondi-Hoyle accretion [39]. Here, we present the first realization of disklike initial conditions in a collisionless scenario, consisting of a three-species (pair-ion) plasma with a significant ion-to-electron mass ratio. With the addition of a strong accretion flow component to the BH magnetosphere in the presented simulation, it becomes possible to better constrain the flaring dynamics of active galactic nuclei (AGN) systems and gain insight into the edge-brightened mechanisms of AGN jets [40–45].

Methods—We use the GRRPIC code `Zeltron` [32,46] to evolve an ion-electron accretion flow combined with a pair-filled black hole magnetosphere. The total simulation domain is denoted by $r \in [0.9r_{\rm h}, 27r_{\rm g}]$ and $\theta \in [0.01\pi, 0.99\pi]$ with a resolution of $N_r \times N_\theta = 1440^2$ for spherical Kerr-Schild coordinates with a grid that is logarithmically spaced in $\hat{r}$ and linearly spaced in $\hat{\theta}$. Here, $r_{\rm g} = GM/c^2$ is the gravitational radius and $r_{\rm h} = (1 + \sqrt{1-a^2})r_{\rm g}$ is the horizon radius, with gravitational constant G, black hole mass M, speed of light c, and dimensionless black hole spin $a = 0.99$. The ion mass is set to $m_i = 100m_e$, where m_e is the electron mass. We initialize a uniform number density, $n = 8n_{\rm GJ}$, wedge that spans $r \in [5, 27]r_{\rm g}$, $\theta \in [\pi/3, 2\pi/3]$, where $n_{\rm GJ} = B_0\omega_{\rm h}/(4\pi ce)$ is the Goldreich-Julian density with angular velocity $\omega_{\rm h} = ac/(2r_{\rm h})$ [47] and B_0 the initial magnetic field strength (see the Supplemental Material [48]). In the inner region, i.e., $r \in [r_{\rm h}, 5r_{\rm g}]$, we initialize a uniform pair-plasma sphere with a number density of $1n_{\rm GJ}$ to kickstart pair production near the black hole. The magnetic field begins as a single large magnetic loop in the poloidal plane (see the Supplemental Material [48]) with an initialized ratio of thermal to magnetic pressure $\beta \in [0.1, 5]$. Our primary focus is investigating the collisionless implications of a persistent MAD accretion state.

The initial configuration of the ion-electron plasma is somewhat arbitrarily chosen and of little consequence to the formation of the relaxed, quasisteady axisymmetric state that is achieved after the simulation has evolved for a sufficient time (see the Supplemental Material [48]). No angular momentum is introduced for the accretion flow at initialization, which expedites the onset of an axisymmetric quasisteady accretion state. However, we note that frame-dragging effects will quickly introduce angular momentum for the innermost black hole regions. For simplicity, we refer to the low angular-momentum accretion flow as the "disk." The ion-electron disk plasma is initialized with a temperature $k_{\rm B}T_{\rm inj} = m_e c^2$ for both ions and electrons. Plasma is replenished from a spherical shell corresponding to $r \in [25, 27]r_{\rm g}$, $\theta \in [\pi/3, 2\pi/3]$, where injection occurs at a fixed rate when the density drops below the initialized disk density. The injection from the boundary emulates the

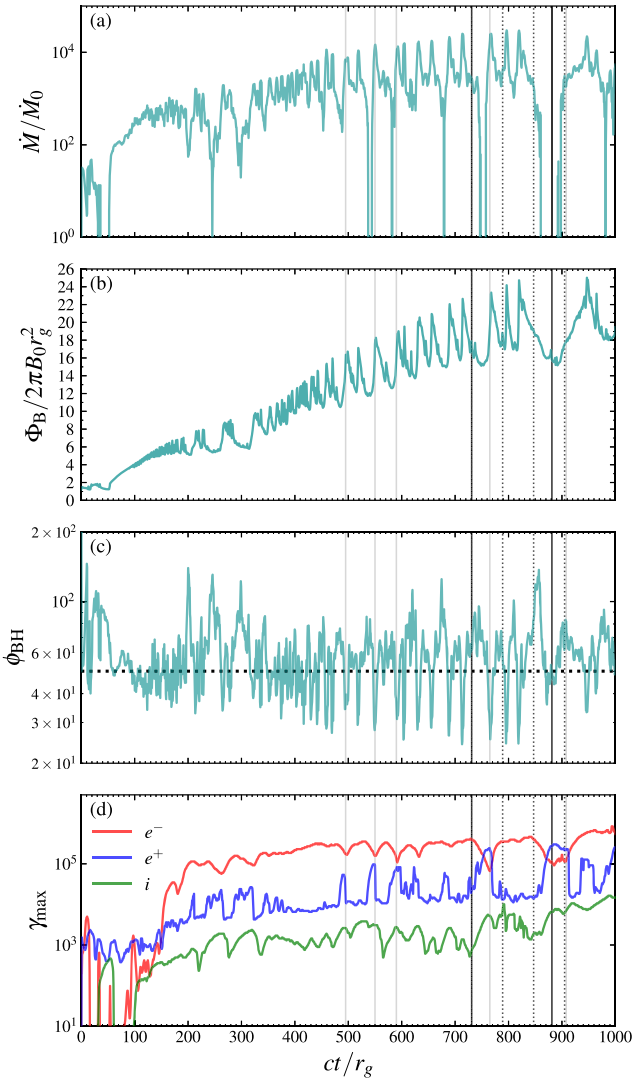


FIG. 1. Time series of the integrated horizon-penetrating fluxes and acceleration of particles. The panels display the (a) combined (i, e^-, e^+) mass accretion rate ($\dot{M}$), (b) horizon-penetrating magnetic flux ($\Phi_{\rm B}$), (c) normalized magnetic flux known as the MAD parameter ($\phi_{\rm BH} = \Phi_{\rm B}/\sqrt{\dot{M}r_{\rm g}^2 c}$), and (d) the maximum Lorentz factor ($\gamma_{\rm max}$; see also Fig. 4) for the three particle species. The horizontal line in panel (c) denotes the theoretically established limit of $\phi_{\rm BH} \sim 50$. The mass accretion rate is normalized with a fiducial quantity defined as $\dot{M}_0 = 0.3cm_i n_{\rm GJ} 2\pi r_{\rm h}^2$. The vertical gray lines mark several times when $\gamma_{{\rm max},e+} \gtrsim \gamma_{{\rm max},e-}$, while the vertical black lines indicate the times displayed in Figs. 2 (solid) and 3 (dotted).

inflow of matter from a large-scale accretion flow. Particles that pass through the outer boundary are removed [49].

Electron-positron pairs are created via photon-photon annihilation of inverse-Compton scattered γ-ray photons with a background photon field [48]. The inclusion of these particle creation effects provides insight into how and if the jet is loaded with pairs and whether these pairs are able to significantly interact at the jet-disk interface. We refer the reader to the Supplemental Material [48] (and Refs. [33,50]) for a more detailed description of the simulation specifics, such as the definition of the poloidal magnetic field initialization, pair production criteria, and characteristic scaling.

Results—The accretion flow dynamic is well summarized in the time series of horizon-penetrating fluxes, where we define the mass accretion rate $\dot{M} = -\iint_A \rho u^r \sqrt{-g} \mathrm{d}\theta \mathrm{d}\phi$ and magnetic flux $\Phi_\mathrm{B} = \frac{1}{2}\iint_A |B^r| \sqrt{h} \mathrm{d}\theta \mathrm{d}\phi$ on the horizon ($r = r_\mathrm{h}$). Here, ρ, u^μ, g, h, and B^r are the mass density, four velocity, metric determinant, spatial metric determinant, and the radial component of magnetic field as seen by local fiducial observers that are normal to spatial hypersurfaces, respectively. The quantity known as the MAD parameter, defined as $\phi_\mathrm{BH} = \Phi_\mathrm{B}/\sqrt{\dot{M} r_\mathrm{g}^2 c}$, is known to saturate at ~ 50 [51]. After it saturates, a flux eruption event occurs, where the magnetic flux is (partially) pushed away from the BH. This leads to a reconnection of the upper and lower hemispheres of the BH magnetosphere in the equatorial plane [29–31], and a resulting drop in Φ_B. We also find that the pairs created by photon-photon annihilation leave an imprint on the system's flux eruptions, as a significant (vacuum) gap can form during the peak of the flux eruption that is rapidly filled by a pair production cascade [Fig. 2(b)].

In Fig. 1, we show direct evidence for a quasisteady axisymmetric MAD accretion state achieved with GRRPIC methods. The top panel clearly outlines sharp decreases in the mass accretion rate $\dot{M}$, which are direct consequences of the flux eruption events, where the accretion flow is temporarily halted because of a magnetic field barrier created by the flux eruption. This relates to the sawtooth structure seen for Φ_B, where the exponential decay is related to the reconnection event (or flux eruption). The general shape of growing Φ_B with the sawtooth structures of $\sim 50 r_\mathrm{g}/c$ in length combined with significant amplitude changes has not been seen before in other GRPIC simulations [cf. [34,39,52]]. The MAD state, corresponding to reaching the limit $\phi_\mathrm{BH} \gtrsim 50$, is established from the very beginning of the simulation. For $T \gtrsim 650 r_\mathrm{g}/c$, we find that both Φ_B and $\dot{M}$ start to saturate.

Figure 2 shows the characteristics of the MAD accretion state in our collisionless simulation. Figure 2(a) shows a still ongoing flux eruption where the accretion flow is

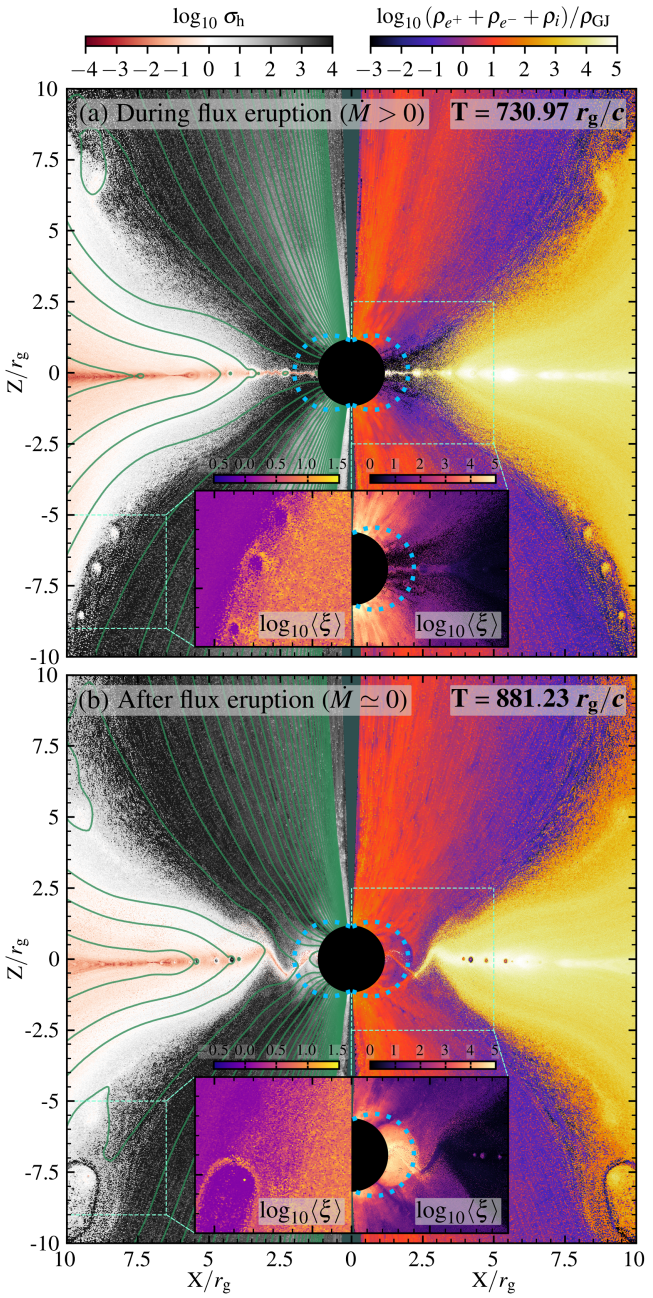


FIG. 2. Overview of the axisymmetric MAD accretion state (a) during ($\dot{M} > 0$) and (b) after a flux eruption ($\dot{M} \simeq 0$). The displayed quantities are magnetization $\sigma_\mathrm{h} = B^2/[4\pi \sum_s \langle\gamma_s\rangle n_s m_s c^2]$, where $\langle\gamma_s\rangle$ is the cell-averaged Lorentz factor and $\rho_s = m_s n_s$ the mass density per species, $s \in \{i, e^-, e^+\}$, normalized with the Goldreich-Julian mass density $\rho_\mathrm{GJ} = m_e n_\mathrm{GJ}$. Kelvin-Helmholtz vortices are seen to form along the jet-disk interface. The inset panels show the density-averaged energy per particle $\langle\xi\rangle = \sum_s \langle\gamma_s\rangle \rho_s c^2 / \sum_s \rho_s c^2$ for different regions of the simulation domain. The *green* contours outline the magnetic flux surfaces. The *dashed blue* contours denote the ergosphere boundary.

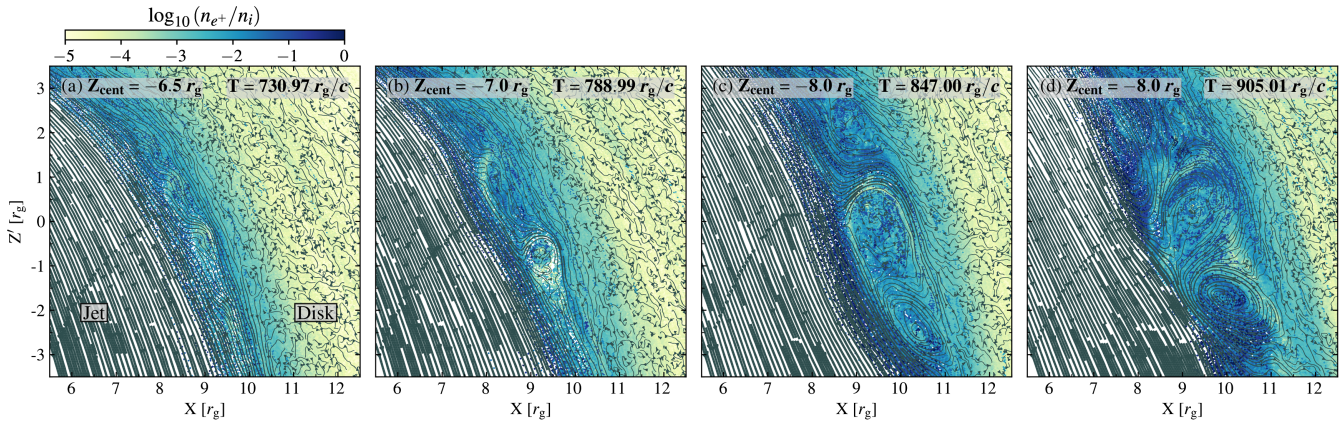


FIG. 3. Growth of a Kelvin-Helmholtz-like mode in the jet-disk boundary over time, where mixing between the disk ions (i) and the jet positrons (e^+) occurs as shown by the number density fraction (n_{e^+}/n_i). The swirl-like motion of the KH vortices is clearly denoted by the three-velocity streamlines. The streamline thickness is scaled according to the magnitude of the velocity. The shown windows are time-averaged over $\Delta T \approx 7 r_g/c$ and centered on (a) $Z_{cent} = -6.5\, r_g$, (b) $Z_{cent} = -7.0\, r_g$. (c) $Z_{cent} = -8.0\, r_g$, and (d) $Z_{cent} = -8.0\, r_g$, respectively.

receding and the magnetic field lines are reconnecting. Figure 2(b) displays the moment when the accretion flow reinstates itself, creating a clear kink in the equatorial current sheet (a manifestation of the relativistic drift-kink instability; [53,54]). The disk-magnetosphere system can be divided into several core regions that are of dynamical interest: (i) the inner *jet*, (ii) the jet *sheath* (i.e., the jet-disk interface), (iii) the equatorial *reconnection* region, (iv) the *inner* (polar) magnetosphere (enclosing the spark gap), and (v) the *disk*. The overdense equatorial plane is in part the result of the enclosing properties of the poloidal magnetic-field loop structure. Moreover, the tearing modes of the equatorial current sheet instigate the creation of pairs, which further contributes to the overdense equatorial plane region. These pairs are created in the vicinity of X-points (locations of significant nonideal electric fields) of the magnetically reconnecting layer, where efficient particle acceleration is known to occur [28,29,55].

Figure 3 highlights that significant velocity shear is found along the jet sheath; associated vortices are similar to those seen for the Kelvin-Helmholtz (KH) instability. The vortices can give rise to magnetic reconnection and subsequent plasmoid formation (shown in a microscopic scenario in [56]). Additionally, it becomes apparent from the n_{e^+}/n_i fraction that significant mixing occurs between matter associated with the jet (i.e., positrons) and matter associated with the disk (i.e., ions), which interface in the jet sheath region. However, the ions do not mix effectively into the inner jet region, as is confirmed in Fig. 3. We also note that the jet sheath layer is quite magnetized with $\sigma_h \approx 1$ (Fig. 2), indicating that magnetic fields are dynamically important.

We find that the flux eruptions occasionally result in the stretching and curling of magnetic fields along the jet sheath. This is caused by an initially nonrotating or slowly rotating magnetic field line that is suddenly set into motion after it enters the BH ergosphere creating a torsional Alfvén wave. The oscillations of the Alfvén wave result in sufficient velocity shear to bring about KH-like behavior. Some of the KH eddies (see also [30]) eventually form circular (island) magnetic field structures [55,57]. These structures then grow via the surrounding swirl-like flows which drag magnetic fields that relax into a circular shell around the original structure.

Figure 1(d) shows the evolution of γ_{max} over time (which is also spatially identifiable with $\langle \xi \rangle$ in Fig. 2), where it becomes clear that $\gamma_{max,e^+} \gtrsim \gamma_{max,e^-}$ during selected flux eruption events (i.e., the vertical lines). These events coincide with the restoration of the accretion flow after a flux eruption. This connects to the findings outlined in Fig. 4 (and the Supplemental Material [48]), where we establish the spatial locations of γ_{max} per particle species. These numbers should be evaluated as a fraction of the maximal Lorentz factor implied by the potential drop $\hat{\gamma}_{max} = eaBr_g/m_e c^2 \simeq 2 \times 10^5$ [32], taking into account the increase in B over time. This is verified in Fig. 1(b) where Φ_B increases ~20 times with respect to the starting value, pushing the simulation closer to a realistic separation of scales. The inner polar magnetosphere regions produce the highest $\gamma_{max} \sim 10^5$ for the electrons and, to a lesser degree, also for the positrons. The ions plateau around $\gamma_{max,i} \sim 10^3$, but they do reach the same total energy when one compensates for the mass difference as $m_i \gamma_{max,i}/m_e \sim 10^5$. We note that γ_{max,e^-} and γ_{max,e^+} can originate in different regions, where the positrons are mainly accelerated in the equatorial reconnection region. The timing of this acceleration coincides with the restoration of the accretion flow after a reconnection event. The pairs created near the X point are collected at the front of the restoring accretion flow. Occasionally, a considerable (vacuum) gap forms on a

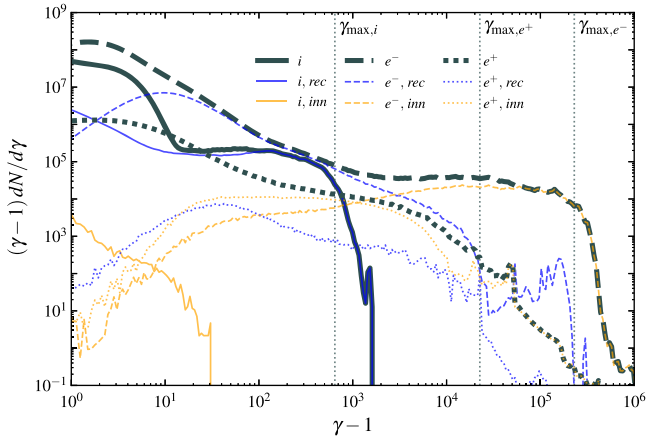


FIG. 4. Two most prominent particle acceleration regions correspond to the equatorial reconnection layer (rec) and inner polar BH magnetosphere (inn). Particle energy distribution from distinct accretion flow regions for the ion (i, solid), electron (e^-, dashed), and positrons (e^+, dotted lines). The thick lines correspond to the spectra calculated for all particles in the $r \leq 25r_g$ domain. The spectra are averaged over the time window $T \in [726.85, 736.14]r_g/c$ corresponding to Fig. 2(a). The vertical lines denote the $\gamma_{\max}$ values that disregard the tail of the distribution. More details of the spectra are outlined in the Supplemental Material [48].

similar timescale, which is rapidly filled with pairs that can then affect and slightly oppose the restoration of the accretion flow [Fig. 2(b)].

The most accelerated electrons originate within and near the ergosphere region where pair creation dynamics associated with spark gaps are known to be important [33]. At the high optical depth to pair creation used here, the gap is small ($\sim 0.01r_g$) and pairs are created in intermittent bursts originating close to the BH that are then accelerated outward (i.e., electrons) or inward (i.e., positrons). Figure 2 shows the two distinct channels for the pair production cascade, which can be advected into the equatorial region [mainly accelerating positrons, Fig. 2(b)] or along the polar (jet) regions [mainly accelerating electrons, Fig. 2(a)]. Especially the equatorial pair cascade (associated with significant unscreened electric fields [48]), creating an equatorial evacuated (*bubble*-shaped) structure [Fig. 2(b)], has not been seen before. For the modest multiplicity pair plasma (i.e., $n_{e^\pm}/n_{\rm GJ} \lesssim 5$), we note that the roles (i.e., inflowing or outflowing) of the leptons are primarily determined by the choice in the sign of $\boldsymbol{\Omega}_{\rm h} \cdot \boldsymbol{B}$; at higher multiplicities, this asymmetry should vanish and polar-cap acceleration should be highly diminished while reconnection-driven particle acceleration should remain mostly unchanged.

Discussion—We have highlighted the complex interplay between accretion-driven behavior, in the form of magnetic flux eruptions, and magnetospheric effects, with the included inverse-Compton scattering and pair production. We identified the most prominent channels of particle acceleration, which are associated with pair production at the polar caps (pairs only) and with magnetic reconnection in the equatorial current sheet (pairs and ions; Fig. 4). Additionally, we find that the jet is loaded with leptons solely created by pair production, and virtually no ions are mixed into it (Fig. 3). Significant mixing between disk and jet matter occurs at the disk-jet interface, primarily because of prominent KH-like modes that grow over time. These modes could lead to additional particle acceleration on the jet-disk boundary on larger scales [56]. The specifics of the gap remain debated [33,50,58–62], but from our simulation it becomes clear that the majority of highly energetic pairs are produced there, where two distinct channels can be identified for our modest multiplicities (Fig. 2). Furthermore, the BH spin influences gap characteristics, warranting further investigation. Future 3D studies will be even more informative on the kinetic effects related to the flux tubes themselves [e.g., [31]].

Conclusion—In this study, we presented the first numerical simulation that combines collisionless accretion (ion-electron disk) and magnetospheric (inverse-Compton scattering and pair creation) effects self-consistently using GRRPIC methods. We highlight the intricate dynamics of a quasisteady MAD accretion state that is currently preferred for several of the most-observed supermassive BH systems [e.g., [7,8]]. The flux eruptions associated with these systems bring about strongly magnetized, largely vacated regions near the central BH, where strong particle-acceleration processes are triggered—mostly in the equatorial current sheet and inner polar magnetospheric regions. The cyclic nature of MAD flux eruptions makes them prime candidates for interpreting the periodic flares of high-energy emission observed from these systems [63,64].

Acknowledgments—The authors acknowledge informative and constructive discussions with F. Bacchini, J. Davelaar, H. Olivares, and C. Gammie. Special thanks are extended to H. Falcke for his support in acquiring the computational resources. This project has received funding from the European Research Council (ERC) under the European Union's Horizon 2020 research and innovation program (Grant Agreement No. 863412). J. V. acknowledges support from the Dutch Research Council (NWO) and SURF which provided the utilized computing resources through Grants No. EINF-7054 and No. NWO-2024.004. B. C. acknowledges computing resources that were provided by TGCC under the Allocation No. A0150407669 made available by GENCI. M. M. and J. V. acknowledge support by the NWO Grant No. OCENW.KLEIN.113. K. P. acknowledges support from the Laboratory Directed Research and Development Program at Princeton Plasma Physics Laboratory, a national laboratory operated by Princeton University for the U.S. Department of Energy under Prime Contract No. DE-AC02-09CH11466.

[1] The collisionless regime refers to the mean free path to Coulomb collisions being large—often exceeding the system size by a multitude of factors [e.g., [65]].
[2] G. G. Madejski and M. Sikora, Annu. Rev. Astron. Astrophys. **54**, 725 (2016).
[3] R. Blandford, D. Meier, and A. Readhead, Annu. Rev. Astron. Astrophys. **57**, 467 (2019).
[4] K. Hada, Galaxies **8**, 1 (2020).
[5] S. Markoff, G. C. Bower, and H. Falcke, Mon. Not. R. Astron. Soc. **379**, 1519 (2007).
[6] H. Falcke, S. Markoff, and G. C. Bower, Astron. Astrophys. **496**, 77 (2009).
[7] EHTC Collaboration, Astrophys. J. Lett. **875**, L1 (2019).
[8] EHTC Collaboration, Astrophys. J. Lett. **930**, L12 (2022).
[9] F. Aharonian *et al.*, Astrophys. J. **636**, 777 (2006).
[10] F. Aharonian *et al.*, Science **314**, 1424 (2006).
[11] J. Aleksići *et al.*, Astron. Astrophys. **544**, A96 (2012).
[12] E. Aliu *et al.*, Astrophys. J. **746**, 141 (2012).
[13] H. E. S. S. Collaboration, Astron. Astrophys. **612**, A9 (2018).
[14] MAGIC Collaboration, Astron. Astrophys. **642**, A190 (2020).
[15] C. B. Adams *et al.*, Astrophys. J. **913**, 115 (2021).
[16] EHT MWLScience Working Group, Astrophys. J. Lett. **911**, L11 (2021).
[17] EHTC Collaboration, Astrophys. J. Lett. **930**, L13 (2022).
[18] H. E. S. S. Collaboration, Astron. Astrophys. **685**, A96 (2024).
[19] I. V. Igumenshchev, R. Narayan, and M. A. Abramowicz, Astrophys. J. **592**, 1042 (2003).
[20] R. Narayan, I. V. Igumenshchev, and M. A. Abramowicz, Publ. Astron. Soc. Jpn. **55**, L69 (2003).
[21] EHTC Collaboration, Astrophys. J. Lett. **910**, L13 (2021).
[22] Gravity Collaboration, Astron. Astrophys. **615**, L15 (2018).
[23] Gravity Collaboration, Astron. Astrophys. **643**, A56 (2020).
[24] M. Wielgus, M. Moscibrodzka, J. Vos, Z. Gelles, I. Martí-Vidal, J. Farah, N. Marchili, C. Goddi, and H. Messias, Astron. Astrophys. **665**, L6 (2022).
[25] J. Vos, M. A. Mościbrodzka, and M. Wielgus, Astron. Astrophys. **668**, A185 (2022).
[26] A. Tchekhovskoy, R. Narayan, and J. C. McKinney, Mon. Not. R. Astron. Soc. **418**, L79 (2011).
[27] J. C. McKinney, A. Tchekhovskoy, and R. D. Bland ford, Mon. Not. R. Astron. Soc. **423**, 3083 (2012).
[28] B. Ripperda, F. Bacchini, and A. A. Philippov, Astrophys. J. **900**, 100 (2020).
[29] B. Ripperda, M. Liska, K. Chatterjee, G. Musoke, A. A. Philippov, S. B. Markoff, A. Tchekhovskoy, and Z. Younsi, Astrophys. J. Lett. **924**, L32 (2022).
[30] J. Davelaar, B. Ripperda, L. Sironi, A. A. Philippov, H. Olivares, O. Porth, B. v. d. Berg, T. Bronzwaer, K. Chatterjee, and M. Liska, Astrophys. J. Lett. **959**, L3 (2023).
[31] J. Vos, J. Davelaar, H. Olivares, C. Brinkerink, and H. Falcke, Astron. Astrophys. **689**, A112 (2024).
[32] K. Parfrey, A. Philippov, and B. Cerutti, Phys. Rev. Lett. **122**, 035101 (2019).
[33] B. Crinquand, B. Cerutti, A. Philippov, K. Parfrey, and G. Dubus, Phys. Rev. Lett. **124**, 145101 (2020).
[34] B. Crinquand, B. Cerutti, G. Dubus, K. Parfrey, and A. Philippov, Astron. Astrophys. **650**, A163 (2021).
[35] B. Crinquand, B. Cerutti, G. Dubus, K. Parfrey, and A. Philippov, Phys. Rev. Lett. **129**, 205101 (2022).
[36] I. El Mellah, B. Cerutti, B. Crinquand, and K. Parfrey, Astron. Astrophys. **663**, A169 (2022).
[37] I. El Mellah, B. Cerutti, and B. Crinquand, Astron. Astrophys. **677**, A67 (2023).
[38] I. Niv, O. Bromberg, A. Levinson, B. Cerutti, and B. Crinquand, Mon. Not. R. Astron. Soc. **526**, 2709 (2023).
[39] A. Galishnikova, A. Philippov, E. Quataert, F. Bacchini, K. Parfrey, and B. Ripperda, Phys. Rev. Lett. **130**, 115201 (2023).
[40] M. Perucho and A. P. Lobanov, Astron. Astrophys. **469**, L23 (2007).
[41] J.-Y. Kim, T. P. Krichbaum, R.-S. Lu, E. Ros, U. Bach, M. Bremer, P. de Vicente, M. Lindqvist, and J. A. Zensus, Astron. Astrophys. **616**, A188 (2018).
[42] M. Janssen *et al.*, Nat. Astron. **5**, 1017 (2021).
[43] A. Pasetto, C. Carrasco-González, J. L. Gómez, J.-M. Martí, M. Perucho, S. P. O'Sullivan, C. Anderson, D. J. Díaz-González, A. Fuentes, and J. Wardle, Astrophys. J. Lett. **923**, L5 (2021).
[44] S. Issaoun *et al.*, Astrophys. J. **934**, 145 (2022).
[45] F. M. Rieger, Universe **8**, 607 (2022).
[46] B. Cerutti, G. R. Werner, D. A. Uzdensky, and M. C. Begelman, Astrophys. J. **770**, 147 (2013).
[47] P. Goldreich and W. H. Julian, Astrophys. J. **157**, 869 (1969).
[48] See Supplemental Material at http://link.aps.org/supplemental/10.1103/5wwb-7t2n for a detailed description of the initial conditions, pair creation mechanisms, scaling conditions, procedure for the spatially decomposed energy spectra, and inner light surface calculations.
[49] B. Cerutti, A. Philippov, K. Parfrey, and A. Spitkovsky, Mon. Not. R. Astron. Soc. **448**, 606 (2015).
[50] A. Levinson and B. Cerutti, Astron. Astrophys. **616**, A184 (2018).
[51] F. Yuan and R. Narayan, Annu. Rev. Astron. Astrophys. **52**, 529 (2014).
[52] A. Bransgrove, B. Ripperda, and A. Philippov, Phys. Rev. Lett. **127**, 055101 (2021).
[53] G. R. Werner and D. A. Uzdensky, J. Plasma Phys. **87**, 905870613 (2021).
[54] G. R. Werner and D. A. Uzdensky, Astrophys. J. Lett. **964**, L21 (2024).
[55] J. T. Vos, H. Olivares, B. Cerutti, and M. Mościbrodzka, Mon. Not. R. Astron. Soc. **531**, 1554 (2024).
[56] L. Sironi, M. E. Rowan, and R. Narayan, Astrophys. J. Lett. **907**, L44 (2021).
[57] L. Sironi, D. Giannios, and M. Petropoulou, Mon. Not. R. Astron. Soc. **462**, 48 (2016).
[58] A. Levinson and F. Rieger, Astrophys. J. **730**, 123 (2011).
[59] A. Levinson and N. Segev, Phys. Rev. D **96**, 123006 (2017).
[60] A. E. Broderick and A. Tchekhovskoy, Astrophys. J. **809**, 97 (2015).
[61] K. Hirotani and H.-Y. Pu, Astrophys. J. **818**, 50 (2016).
[62] A. Y. Chen and Y. Yuan, Astrophys. J. **895**, 121 (2020).
[63] K. Dodds-Eden *et al.*, Astrophys. J. **698**, 676 (2009).
[64] GRAVITY Collaboration, Astron. Astrophys. **638**, A2 (2020).
[65] R. Fitzpatrick, *Plasma Physics: An Introduction (1st ed.)* (CRC Press, Boca Raton, 2014).